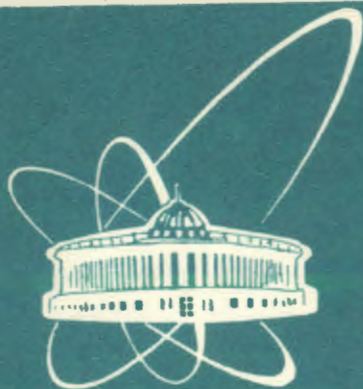


93-384



ОБЪЕДИНЕННЫЙ
ИНСТИТУТ
ЯДЕРНЫХ
ИССЛЕДОВАНИЙ
ДУБНА

E1-93-384

S.V.Andreev, S.B.Vorozhtsov, S.I.Kakurin,
V.G.Krivokhizhin, L.A.Merkulov, Yu.L.Obukhov,
V.A.Panacik, I.A.Savin, A.A.Festchenko,
Yu.A.Shishov, I.P.Yudin

SOME CHARACTERISTICS
OF THE SUPERCONDUCTING
MAGNETIC SYSTEM
OF TOROIDAL SPECTROMETER STORS

Submitted to «Nuclear Instruments and Methods»

1993

INTRODUCTION

As is known, lepton deep inelastic scattering of different targets is the simplest method to study the nucleon and nuclei structure because all the relevant information can be obtained from characteristics of incident and scattered leptons. After the experiments on deep inelastic scattering at SPC, CERN and FERMLAB, it has become clear that further studying of nucleon structure at fixed targets with energies up to 2000 GeV (SPC, CERN, FERMLAB, UNK) together with the rise of statistics, requires a substantial decrease of systematic errors.

The spectrometer with a toroidal magnet of a distributed type, used successfully by the BCDMS collaboration^[1], is the most convenient for this purpose because of:

- high (70–100%) and homogeneous efficiency up to the maximum possible values of Q^2 ;
- a long target which guarantees high luminosity of the set-up and large statistics data;
- the possibility of simultaneous data collection with different targets that sufficiently decreases systematic errors of measurements.

But, on the other side, the main restrictions of the toroidal spectrometer with the iron magnet are:

- a relatively poor resolution;
- difficulties to fulfil calibrations.

The progress of the recent times in the development and production of the superconducting magnetic systems, allows one to create air gap superconducting toroidal magnets. They are free at material along the scattered muon trajectories, provide quite a large value of the field integral and accurate calibration of the spectrometer. So, they release the main restrictions of the iron toroids.

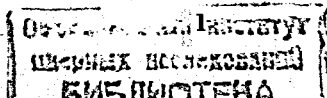
There is a suggestion to construct the superconducting toroidal spectrometer (STORS)^[2] for precise measuring of the structure functions in muon beams at the highest energies. A scheme of such a spectrometer is presented in Fig.1. The basic element of this spectrometer is a superconducting magnetic system consisting of a superconducting toroidal magnet and subsystems: electric supply and protection, cryogenics, vacuum, automatic measurements, check-up and control.

In this paper we present the description of the magnet construction (section 1); calculation of the magnetic induction and forces influencing the elements of the magnet (section 2); requirements to the reliability and rigidity of the carrying elements of the magnet construction (section 3), and the calculations for strength and stiffness of the carrying construction elements of STORS (section 4).

1. SUPERCONDUCTING MAGNETIC SYSTEM

1.1. THE SCHEME OF THE SYSTEM

The superconducting magnetic system (SCMS) consists of a superconducting toroidal magnet (SCTM) and subsystems: electric supply and protection, cryogenics, vacuum, automatic measuring, check-up and control.



The approximate sizes and main parameters of the SCTM are presented in Figs.2, 3 and in Table 1. The SCTM consists of three modules, 12 meters long, each 5 m in outside diameter. The two first modules (from the input of the primary muon beam) have the inner aperture of radius ≈ 0.54 m, and the last one ≈ 0.2 m.

Every module has eight equaled square coils connected with the force rod into the unified toroidal construction (Fig.2). The side view of the module is shown in Fig.3A, the cross-section of the coil is given in Fig.3B. The conductor (1) is laid into box (2) placed in the vacuum vessel (3). The outside heat flow is restricted by the multi-layer vacuum isolation or carbon screen (4). The coil consists of several tens of the conductor (1) turns and everything is united with the epoxide compound in box (2) together with pipe (5) to be cooled by helium. Radial pondermotor forces pushing the coil, are accepted by rods (6). In the third module the parts of the coil closest to the module axis, are supported by the force tube. The modules are also connected between themselves by "cold" force rods. The boxes of the coils are hung inside the vacuum vessel, for example, with the tangential rods placed near the outside force rods (it is not shown), there are sixteen rods at every end of the module. The front part of the coils of the first module, is kept from moving in the longitudinal direction with the help of eight or sixteen longitudinal force rods placed along the horizontal part of the coils inside the vacuum vessel.

1.2. CONDUCTOR

The construction and parameters of the tire, are represented in Fig.4 and Table 2. The transported contact arm consisting of the wires of diameter $8.5 \cdot 10^{-4}$ m, is stabilized with highly pure aluminium. The connection of the superconductors with the aluminium matrix is obtained either in the process of joint extrusion or soldering. The number of the wires of diameter $8.5 \cdot 10^{-4}$ m, is chosen taking into account the maximum value of the induction B_{max} in the coil. The calculations given below (see part 2), have shown that in the first two modules $B_{max} = 3.6$ T, in the third one — $B_{max} = 4.3$ T. Here these values have been obtained at the condition that the current is concentrated in the wires $8.5 \cdot 10^{-4}$ m in diameter, i.e. at the width of the transported tire. If the current is considered to be distributed along all the contact arm ($3.08 \cdot 10^{-2}$ m in this case), then B_{max} values become sufficiently smaller. Then we consider that the critical current of the contact arm should be approximately twice as high as the nominal current. This provides a higher reliability of the magnet operation.

The length of the wire getting into SCTM (3 modules) $8.5 \cdot 10^{-4}$ m in diameter, is 1.45 thousand kilometers. Taking into account technological throws (fabricating contact arm, at first twisted and then stabilized) and losses, it is necessary to get, approximately, by 25% more, i.e. 1.8 thousand kilometers (Table 3).

The weight of the contact arm 48 km long, getting into the magnet, is approximately 19 tons, in the 55 km being ordered ≈ 22 tons. With 10% technological storage, the necessary weight of the aluminium will be 17 tons.

1.3. SUBSYSTEMS

1.3.1. ELECTRICITY AND PROTECTION SOURCE

The principal scheme of the subsystem is presented in Fig.5. The parameters of the electric source: maximum current 12.5 kA, power 48 V.

The construction of the electricity protection is represented with the detector (6) of appearance of the normal zone in the coil of the magnet (5), two commutators of force currents (2) and (3) and resistivity absorbers (4) of the stored energy in the magnet. Tiristoral and vacuum switchers can be used as commutators.

1.3.2. CRYOGENIC VACUUM SUBSYSTEMS

The principal technological scheme of the cryogenic and vacuum systems SCMS is presented in Fig.6.

A CHS-1600/4.5 cryogenic helium set-up of the power 1600 W is supposed to be used. If necessary, additional liquid helium will be given from the vessels of the total volume 10 m^3 .

1.3.3. AUTOMATIC SYSTEMS OF MEASURING, TESTING AND CONTROL

The automatic system of control based on a PC of the IBM AT 386 type, should promote reliability in SCTM exploitation at minimum expenses.

TABLE 1

MAIN PARAMETERS OF THE MAGNET

Number of coils in the magnet	8
Module length	12 m
Coil maximum radius	2.5 m
Coil minimum radius for	
module of the 1st type	0.54 m
module of the 2nd type	0.2 m
Layer number of the aluminium tire in the cross-section of the coil	70
Aluminium tire thickness	$4.4 \cdot 10^{-3}$ m
Aluminium tire width	$3 \cdot 10^{-2}$ m
Thickness of the superconducting layer of tire	$1.7 \cdot 10^{-3}$ m
Width of the superconducting layer of tire for	
module of the 1st type	$12.3 \cdot 10^{-3}$ m
module of the 2nd type	$14.0 \cdot 10^{-3}$ m
Curvity inside radius of the curved parts of the coil	0.5 m
Current power in the coil	700 kA
Distance between the modules	0.7 m
Number of the 1st type modules	2
Number of the 2nd type modules	1
Maximum induction in the coil	
of the 1st type modules	3.6 T
of the 2nd type modules	4.3 T
Length of the contact arm in the module	16 km
Length of the contact arm in the magnet	48 km
Number of the conductors	
in the module of the 1st type	29
in the module of the 2nd type	33
Length of the conductor	
in the modules of the 1st type (2×460 km)	920 km
in the modules of the 2nd type	530 km
Length of the conductor in the magnet	1450 km

TABLE 2

CONDUCTOR PARAMETERS

Sizes of the contact-arm cross-section	
without isolation	$(4 \times 30) \cdot 10^{-6} \text{ m}^2$
with isolation	$(4.4 \times 30.4) \cdot 10^{-6} \text{ m}^2$
Stabilizing aluminium	99.995%
Critical current	20 kA
Conductor diameter	$8.5 \cdot 10^{-4} \text{ m}$
Number of conductors	
in the 1st type module	29
in the 2nd type module	33
Number of veins in the conductor	2970

TABLE 3

MAIN ASSUMPTIONS MADE WHILE CALCULATING THE QUANTITY OF THE CONDUCTOR OF DIAMETER $8.5 \cdot 10^{-4} \text{ m}$

Critical conductor current at the maximum induction in the coil	
of the 1st type module at 3.6 T	700 A
of the 2nd type module at 4.3 T	600 A
Relation of the critical and nominal currents in the contact arm	2
Length of the contact arm in the magnet	48 km
Length of the ordered contact arm (supply 15%)	15 km
Conductor length in the magnet	1450 km
Length of the ordered conductor ($1450 \text{ km} \times 1.25$)	1800 km

2. CALCULATION OF MAGNETIC FIELD AND PONDERMOTOR FORCES IN CURRENT CARRYING CONSTRUCTIONS

2.1. CALCULATION METHOD

The base of evaluation program of space magnetic field distribution is structure sub-routines from program collection MAGSYS^[3] able to evaluate field investment of straight- and curve-line bars with the rectangular cross section. But we calculate the field of current winding as a sum of investments from each region, and every investment is represented analytically by Biot-Savart's law. The curve-line region was approximated by the broken line, consists of six straight-line regions. The MSTORS subroutine calculates the summary field of all magnet current regions. We plan to coordinate a straight-line division with the necessary accuracy of field evaluations near that curve-line bar.

2.2. MAGNETIC FIELD OF SPECTROMETER

During the investigations, two variants of superconducting ironless magnets were considered. All the spectrometer machine consists of these two various types of magnet modules. The characteristics of the magnets are represented in Table 1.

The radius distribution of azimuthal magnetic field component is presented in Figs.7,8 with different angle for the both variants of modules.

It seems that the azimuthal field heterogeneity has a significant value near the conductor with current. This circumstance leads to difficulties in experiment results processing and increases calculation time for every event.

A simple method to improve azimuthal field homogeneity is increasing the number of windings. If we increase the number of windings from 8 to 12, the field dispersion will be improved by 25-50% for the azimuthal component (the mean value remains invariable), and by 20-30% for the radius component (the mean value is decreased). Nevertheless, the tendency to have the maximum value of acceptance and minimum cost of magnets, limits the number of windings.

The space distribution of B_ϕ and B_r components is presented in Figs.9,10. Remarkable heterogeneity appeared in the regions directly near the current winding.

There are the most heterogeneous sections of the magnetic field components in the boundary modules regions, see Figs.11-13. These figures correspond to the beginning of working region by ϕ , due to the winding decreasing the working region.

If we consider the field outside the module, we see a sharp slump of the field value along both radius and axis z . This is seen in Figs.14,15.

According to [2], the field calibration must have an accuracy more than $3 \cdot 10^{-4}$. Therefore calculations of the final field map for experimental processing has a double precision. As for the complete field map including three modules, 90 hours of calculation are needed for VAX-8350.

Figs.16,17 show integral characteristics for B_ϕ component along ϕ and z .

2.3. CALCULATION OF PONDERMOTOR FORCES AT WINDING

The calculation of forces acting on winding was made with definition of the forces sum of all the winding tires and by the full cross-section of winding represented as a solid superconducting tire.

If we define the main characteristics of the magnetic field component distribution, this approach is also correct. The character of the distribution of all the field components and acting pondermotor forces will not be changed, but the real field must be determined with the necessary precision to eliminate sources of systematic errors.

Table 4 shows the values of pondermotor forces acting per meter in straight-line axial and radial regions of winding for the case where the distance between the modules is 0.3 m. The place of force arising and the directions of these forces are shown in the scheme of mutual disposition for three magnet modules of the spectrometer (see Fig.18).

TABLE 4

f_1	f_2	f_3	f_4	f_5	f_6	f_7	f_8
0.51	0.19	1.02	0.35	0.37	0.332	0.331	0.35

As for the radial winding parts, they expose heterogeneous efforts along all the segment. This is associated with heterogeneous distribution of the field along the radius of the module. As a rule, these efforts at the bound of the radial straight-line segments are increasing by 40–80% in comparison with the efforts at the centers of the segments. Table 4 indicates averaging along the length value of the forces acting per radial segment unit.

Curve-line segments are more strained from the angle arising pondermotor forces. The maximum value of these forces is 1.37 times higher than that of the forces at the center of straight-line segments. For the first type of the module there are the following values of field tension for the axis nearest to the axial segment: a) on the external tire surface from axis — 1.773 T; b) on the internal tire surface — 3.129 T.

The corresponding tensions for the curve segment near this axial segment will be: a) on the external surface — 1.65 T; b) on the internal surface — 3.341 T.

For the axial segments of the second type of module, these values will be 1.27 T and 3.72 T.

These values (maximum tension 3.72 T specially) are needed to choose critical current value in the superconductor. Knowing the critical current, we have got the necessary amount of the superconductor for winding. The absolute maximum value of the field component for the inside axial part of the winding, may be estimated from Fig.19.

The field of each module distorts the field of the others, disposed at a distance 0.3–0.7 m between them. The sum field is decreasing in comparison with the field of each module. This leads to the repellent effect between the modules.

If we increase the distance to 0.5 m, the effect is decreasing approximately threefold.

Besides, the sum forces acting on external and internal straight-line axial segments, are directed to the center. These forces are equal to 3.33 MN for the first type of the modules and 8.63 MN for the second type.

2.4. EVALUATION OF ARISING FORCES UNDER CONSTRUCTIVE ERRORS

The azimuthal forces acting on winding are equal to zero, due to the modules' symmetry. Winding of tire layers was assumed to be ideal. But if there is a small displacement of any layer at the upper or lower axial segment, these forces will be present. For a displacement 0.002 m, the azimuthal forces will be 0.0629 MN. It is necessary to emphasize that nonsymmetry deviations of assembling process lead to a growth of the azimuthal forces. The lower straight-line axial part of winding is in the most strained condition. Depending on the character of deviations the situations can be as follows:

1. under the deviation of the winding plane around the magnet axis by $\alpha = 0.1^\circ$ (see Fig.20B) the maximum deviations of the lower part of winding compared with the ideal one will be $1.45 \cdot 10^{-3}$ m and the arising azimuthal force will be $1.2 \cdot 10^{-3}$ MN/m;
2. at the curving of lower axial part of winding by $\beta = 1^\circ$ (see Fig.20C) the maximum deviation will be $2.42 \cdot 10^{-3}$ m and the arising azimuthal force will be $0.8 \cdot 10^{-3}$ MN/m;
3. under the combined upper deviations (see Fig.20D) the maximum deviations of the lower part of winding will be $3.87 \cdot 10^{-3}$ m and the arising azimuthal force will be approximately equal to the sum of forces $2.06 \cdot 10^{-3}$ MN/m.

Any other combinations of deviations are practically a sum of the acting azimuthal forces.

The other kinds of deviations under the magnet construction will result in changing the value of the magnetic field in all the magnet region. It is desirable to evaluate the degree of changing of magnetic field component ($\eta = dB_\varphi/B_\varphi$) because there are strict requirements for the accuracy of this field. Preliminary estimations have shown that most of the modifications of the magnetic field are caused by deviations connected with the lower axial part of winding. For the first approach, the value of changes of the magnetic field is proportional to the value of deviations. We represent the following cases:

1. There is an increase of the radial size of winding by value $2 \cdot 10^{-3}$ m. The character of the relative changing of the field for this case is in Fig.21, and quantitative values of these changes may be evaluated from Figs.22, 23;
2. There is a displacement of the lower axial part of winding along the radius by value $2 \cdot 10^{-3}$ m (see Fig.20A). The power of the relative changing of the field is presented in Fig.24, the quantitative estimations of these changings are in Figs.25, 26;
3. There is a shift of the winding plane by an angle $\alpha = 0.135^\circ$ (see Fig.20B) that corresponds to the maximal displacement of the edge of the lower part of winding by value $2 \cdot 10^{-3}$ m. The character of the relative changing of the field is given in Fig.27, the quantitative estimations are in Figs.28, 29.
4. There is bending of the lower straight-line segment of winding near its own axis by an angle $\beta = 0.744^\circ$ (see Fig.20C), that corresponds to the maximal displacement of the edge of this segment of winding by value $2 \cdot 10^{-3}$ m. The picture of the arising relative changes of the field is in Fig.30, and quantitative estimations are in Figs.31, 32;
5. There are non-parallel upper and lower straight-line axial segments of winding, and the displacement between the edges is $2 \cdot 10^{-3}$ m. The general picture of the arising relative changing of the field at the median plane is shown in Fig.33, and quantitative estimations are given in Figs.34, 35.

2.5. THE MAGNETIC FIELD APPROXIMATION OF STORS

To use a magnet, it is necessary to know the value of the field at any point of the magnet working region. The initial calculation subroutine gives us some grid of the field values and the calculation time per point is 10 seconds. Due to that it is needed to find the rapid approximation of the magnetic field according to the discreet value grid. It was tested in the Chebyshev interpolation and cubic spline interpolation. There are subroutines to evaluate the magnetic field at any working region. Also the accuracy and the calculation time have been estimated.

2.5.1. GRID OF MAGNETIC FIELD

The initial data for the approximation represented by three components of vector (B_x , B_y , B_z) on the non-equidistant grid of the polar coordinates are φ , z , r (i.e. angle, axis displacement, normal axis displacement).

Nodes for axis z are $z = 0$; $0.7 \div 4.9$; 4.9 ; $5.15 \div 5.4$; 5.4 ; $5.45 \div 6.0$ (m).

Nodes for axis φ are $\varphi = 0^\circ$; 0.25° ; 0.5° ; 1.0° ; 1.5° ; 2.0° ; 2.5° ; 5.0° ; 7.5° ; 12.5° ; 17.5° and 22.5° .

Nodes for axis r are varied depending on φ and z :

1) $0^\circ \leq \varphi \leq 2.5^\circ$

- I $0.3 \text{ m} \leq r < 1.0 \text{ m}$, step 0.01 m;
- II $1.0 \text{ m} \leq r < 1.8 \text{ m}$, step 0.10 m;
- III $1.8 \text{ m} \leq r < 2.1 \text{ m}$, step 0.05 m;
- IV $2.1 \text{ m} \leq r \leq 2.5 \text{ m}$, step 0.01 m;

2) $5^\circ \leq \varphi \leq 22.5^\circ$

- I $0.3 \text{ m} \leq r < 1.0 \text{ m}$, step 0.02 m;
- II $1.0 \text{ m} \leq r < 1.8 \text{ m}$, step 0.10 m;
- III $1.8 \text{ m} \leq r \leq 2.5 \text{ m}$, step 0.02 m.

2.5.2. FIELD APPROXIMATION BY CHEBYSHEV'S POLYNOMS

A usual B_y magnetic field type is represented in Fig.36. Finding approximation is zone depending on every component. It is easy to distinguish three peak regions in Fig.36. If we approximate the whole definition region of the field by one Chebyshev's polynomial, we find the greatest error in these regions. Due to that, every peak region is processed separately. The field without these peaks is smoothed and thereby it is one more part for processing. In this way we save machine memory without decreasing the accuracy compared with a simple method of divided regions. Also every separated region is limited by the value of φ , because of the large angle peak decreasing. The B_x field component was processed in analogous way. For this case we can distinguish two peak regions. The B_x component has the following regions — the peak and the plane. The plane region is represented by the low degree polynomial and so we decrease the previous calculation errors (zero oscillations).

The main difficulty to calculate the necessary degree of decompositions at the known precision, is the processing of the radius dependence. For various degrees of the decomposition for all the working region without peaks, the following result was obtained. For degree 20 the order of relation error is $10^{-1} \div 10^{-2}$; for degree 40: $10^{-2} \div 10^{-3}$; for degree 70: 10^{-4} .

2.5.3. ACCURACY OF THE APPROXIMATION AND THE CALCULATION TIME

To evaluate the calculation time Chebyshev's decompositions of $15 \times 15 \times 35$ degree for the first, second and third axes were used. The finding time per every three-dimensional count is 0.35 second.

In conclusion we can say that for certain precision 10^{-4} the calculation time will be approximately 3.5 seconds (from the needed number of coefficients $0 \div 35 \times 0 \div 35 \times 0 \div 70$). The time for cubic spline interpolation is 2.5 seconds. The data amount is nine regions with sets $36 \times 36 \times 71$.

3. CHOICE OF THE ADMITTED STRESSES AT THE POWER FRAMEWORK AND WINDING

It is proposed to manufacture the elements of power framework (cradles and frames) from aluminium alloy AMg6 with a strength stress $\sigma_b = 560 \text{ MPa}$ for a temperature of 4.2 K and with a yield stress $\sigma_{0.2} = 200 \text{ MPa}$. In the general machine-building the coefficients

of strength reserve correlated for the value $\sigma_{0.2}$, $n = 1.5^{[5]}$ have been obtained. Then the average value of the admitted stress is $\sigma_a = \sigma_{0.2}/n \approx 130 \text{ MPa}$. The deformation of the framework creates the stress in winding that consists of superconducting wires, stabilizing tire of high-purity aluminum, electrical insulation and impregnating compound. For that system the stress in winding elements must not cover the allowed limits considered below.

3.1. SUPERCONDUCTOR

The stretching stress in the wire with Nb-Ti vein and Cu matrix decreases the critical current. But it will be noticeable under great stress. For example, the critical current decreases by approximately 5% for the multi-vein wire at an induction of 4 T and a stress of 500 MPa. The author of the work [6] believes that the right value for the maximum work stress for a Nb-Ti wire, is 500 MPa.

3.2. MATRICES OF THE TIRE

Pure aluminum (for example 99.995%) is used as stabilizing tire material. The specific electrical resistance of that aluminum is $\rho \approx 5 \cdot 10^{-11} \text{ Ohm} \cdot \text{m}^{[7]}$, for a temperature of 4.2 K and without any deformations. The correlation of the specific resistance is

$$RRR = \rho(300\text{K})/\rho(4.2\text{K}) \approx 2.8 \cdot 10^{-8}/5 \cdot 10^{-11} = 560.$$

But the value of ρ depends on the power of deformation, and for the relative strain $\epsilon = 0.07$, ρ will be $\approx 1.2 \cdot 10^{-11} \text{ Ohm} \cdot \text{m}$. For that value of ϵ the stress must be $\sigma \approx 100 \text{ MPa}$. It means that to preserve the power of stability it is needed to increase the cross-section 2.4 times. If the 25% increase of ρ is admitted, then the strain of the construction must be $\epsilon \approx 0.03$ that corresponds to the value $\sigma \approx 50 \text{ MPa}^{[7]}$.

The mentioned above stresses and strains are in the plastic region. After a great number of cycles of the plastic deformation, the yield stress will grow^[6], but as earlier it remains rather low. And what is more, electric resistance essentially increases^[7].

For more pure aluminium ($RRR=2000$), the sharp growth of the resistance begins even at $\epsilon = 0.003$, but after multicycling (Fig.39)^[8].

3.3. ELECTRICAL INSULATION AND COMPOUND IMPREGNATING THE TIRE

Traditionally fiberglass and epoxide resin are used to perform impregnation of the tire, and as a result the coils of the conductor will be monolith analogously to glasstextolite for insulation of the wire. It seems that the mechanical properties of that composite are analogous to those of ordinary glasstextolites. For example, the breaking stress under static bending perpendicular to layers for sheets of type ST glasstextolites with thickness 0.01 m and more at normal temperature along the basis of fabric, is 125 MPa and along the weft of fabric — 95 MPa. For STEF-1 type these values are 360 and 300 MPa. The breaking stress for the stretching of the ST type are 90 and 70 MPa. The modules of elongation for bending various at width range accordingly to the initial materials and construction technology, and these values for example are (15.6-32) GPa for different correlations of the amount of fiberglass and epoxide resin^[10].

3.4. DISCUSSIONS AND CONCLUSIONS

Let us find the stress in the cradle, when the growth of electrical resistance in the aluminium matrix of the tire is admitted. As was mentioned above, we suppose the allowed relative lengthening is $\epsilon = 0.03$, when both the cradle and the winding are bent. The value of the normal stress under bending of the cradle varies along the section according to the linear law. As the correlation of the cross-section heights of the cradle and the winding is $450/300=1.5$, then the value along the edges of the cradle is allowed to be equal to $\epsilon = 0.03 \times 1.5 = 0.045$. According to Hooke's law, the stress at the point is

$$\sigma = E \cdot \epsilon = 80 \cdot 10^4 \times 0.045 = 3.6 \text{ GPa,}$$

where E is the modulus of elongation of the aluminium alloy. It is obvious that the real stress in the cradle will be less by an order, consequently, the strain of the winding will be less by the same factor, too. Even for aluminum with a relative resistance 2000, at $\epsilon = 0.003$, the allowed value is $\sigma = 360 \text{ MPa}$. Thus, aluminium matrix is not an obstacle to essential loading of the cradle.

The electrical insulation and compound impregnating may be a weaker link. If we orient ourselves to the minimal value (70 MPa) of breaking stress while stretching ST glasstextolite and the reserve coefficient is 1.4, then the allowed stress in the insulation of the winding will be $\sigma_{in} = 50 \text{ MPa}$. For the same power of strain of the insulation and the cradle, the stress in the cradle is $\sigma_{cr} = \sigma_{in} \cdot (E_{cr}/E_{in})$.

Let $E_{in} = (15.6 + 32)/2 \approx 24 \text{ GPa}$, then $\sigma_{cr} = 50 \cdot 80/24 \approx 170 \text{ MPa}$, at a distance of 0.15 m from the center of section of the cradle, and $\sigma_{cr} \approx 250 \text{ MPa}$ at the edges of the cradle.

We can conclude that choosing the values of the allowed stress in the power framework we can use the principles of general machine-building, because while winding the negative phenomena appear at an essentially greater stress.

4. CALCULATIONS FOR STRENGTH AND STIFFNESS OF CARRYING CONSTRUCTION ELEMENTS OF STORS

4.1. CALCULATIONS FOR STRENGTH AND STIFFNESS OF CARRYING CONSTRUCTION ELEMENTS OF THE MAGNET

All the elements of the cold part of the magnet are fabricated of aluminium alloy AMg6. The cradle fixes the winding wrapping it from all the sides with two L-like in cross-section parts. One part of the cradle is used as a mould to cover the winding (Fig.40). To fix cradles respecting each other, 8-angle frames are used (see Fig.41).

4.1.1. CRADLE

To check the construction for strength and stiffness, it is necessary to know the value of the maximum stress arising at the cross-section of the cradle, the value of the deflections of winding at the straight-line segments and the strain of the bar of the magnet connecting frames.

As seen from Fig.42, the maximum value of the distributed loading at the internal straight-line part of the first type module winding, is 510 kN/m, for the second type 1020 kN/m; for the external part of the both types of modules 190 kN/m, and for the radial part 370 kN/m.

To protect the construction from damage, the cradles are placed on 11 supports at an interval of 1 m from each other for the first type modules and on 14 supports at 0.8 m for the second type modules.

The cradle cross-section $F = 2.26 \cdot 10^{-2} \text{ m}^2$ (Fig.40).

Centroidal moment of inertia:

$$J_x = bh^3/12 - b_1h_1^3/12, \quad J_x = 3.28 \cdot 10^{-4} \text{ m}^4.$$

Section modulus:

$$W_x \approx 2J_x/h, \quad W_x = 1.6 \cdot 10^{-3} \text{ m}^3.$$

In Fig.43 the equivalent scheme of the loading of the internal and external straight-line parts of winding is represented. These parts are considered as multispan girders with distributed loading q . While calculating strength and stiffness of these girders, the bending moments, the reaction at the support and the flexures of one-piece girders with equal spans l long, were found according to the formulae from work [11] with coefficients from Table 13^[11].

When calculating, we consider the edging spans to be on the mobile supports, but all the intermediate spans are rigidly fixed at the ends.

First type modules:

$q = 510 \text{ kN/m}$, gird is kept with 11 supports, $l = 1 \text{ m}$.

The bending moments are:

$$M_{1,10} = 0.08ql^2, \quad M_{1,10} = 420 \cdot 10^3 \text{ MN} \cdot \text{m}, \quad M_{2+9} = 0.025ql^2, \quad M_{2+9} = 130 \cdot 10^3 \text{ MN} \cdot \text{m}.$$

The maximum stresses are:

$$\sigma_{max} = M/W_x, \quad \sigma_{max1,10} = 26.6 \text{ MPa}, \quad \sigma_{max2+9} = 8.4 \text{ MPa}.$$

The maximum deflections are:

$$f_{1,10} = 0.0068ql^4/EJ_x, \quad f_{1,10} = 1.5 \cdot 10^{-4} \text{ m}, \quad f_{2+9} = 0.0005ql^4/EJ_x, \quad f_{2+9} = 1 \cdot 10^{-5} \text{ m},$$

where E — Young's modulus, for AMg6 $E = 7 \cdot 10^4 \text{ MPa}$.

Second type modules:

$q = 1020 \text{ kN/m}$, gird is kept with 14 supports, $l = 0.8 \text{ m}$.

The bending moments are:

$$M_{1,13} = 0.08ql^2, \quad M_{1,13} = 550 \text{ MN} \cdot \text{m}, \quad M_{2+12} = 0.025ql^2, \quad M_{2+12} = 170 \text{ MN} \cdot \text{m}.$$

The maximum stresses are:

$$\sigma_{max1,13} = 35.7 \text{ MPa}, \quad \sigma_{max2+12} = 10.9 \text{ MPa}.$$

The maximum deflections are:

$$f_{1,13} = 0.0068ql^4/EJ_x, \quad f_{1,13} = 1 \cdot 10^{-4} \text{ m}, \quad f_{2+12} = 0.0005ql^4/EJ_x, \quad f_{2+12} = 8 \cdot 10^{-6} \text{ m}.$$

The external segment part of modules of any type with loading $q = 190 \text{ kN/m}$ and resting on 11 supports, $l = 1 \text{ m}$.

The bending moments are:

$$M_{1,10} = 0.08ql^2, \quad M_{1,10} = 150 \text{ MN} \cdot \text{m}, \quad M_{2+9} = 0.025ql^2, \quad M_{2+9} = 50 \text{ MN} \cdot \text{m}.$$

The maximum stresses are:

$$\sigma_{max1,10} = 9.8 \text{ MPa}, \quad \sigma_{max2+9} = 2.6 \text{ MPa}.$$

The maximum deflections are:

$$f_{1,10} = 0.0068ql^4/EJ_x, \quad f_{1,10} = 4 \cdot 10^{-5} \text{ m}, \quad f_{2+9} = 0.0005ql^4/EJ_x, \quad f_{2+9} = 3 \cdot 10^{-6} \text{ m}.$$

The radial parts of magnet winding have length of straight-line part $l = 1.2 \text{ m}$ with distributed loading = 370 kN/m. The equivalence scheme of loading is represented in Fig.44, where the ends of girders are rigidly fixed.

The bending moment is:

$$M \approx ql^2/8, M = 760 \text{ MN}\cdot\text{m}.$$

The maximum stress is:

$$\sigma_{max} = 49 \text{ MPa}.$$

The maximum deflection is:

$$f = 5ql^4/384EJ_x, f = 3 \cdot 10^{-4} \text{ m} [12, \text{p.53, Table 10}].$$

From calculation for strength and stiffness we see that the maximum value of stress in the winding cradle $\sigma = 49 \text{ MPa}$ arises at radial parts of the winding.

The elements of the cold magnet part are made of material that can have reticent defects, technological errors and other factors influencing the construction strength. Due to that, it is needed to set the reserving strength coefficient n_b .

Selection of n , showing how many times the admitted stress σ_a is lower than the danger stress, depends on the condition of the material (fragile, plastic), character of load acting (static, dynamic, cyclical). Also, the selection depends on material heterogeneity, errors of the external loadings being determined, proximity of calculation schemes and formulae. The danger stress for plastic materials under static loading is equated to yield stress of material $\sigma_{0.2}$ and $n_{0.2}$ is assumed $n_{0.2} = 1.4 \div 1.6$. Sometimes the admitted stress for plastic materials is defined by strength stress $\sigma_a = \sigma_b/n_b$. As $\sigma_{0.2} = (0.5 \div 0.7)\sigma_b$, then $n_b = 2.4 \div 2.6$. The yield point of AMg6 is $\sigma_{0.2} = 160 \text{ MPa}$, the strength stress is $\sigma_b = 320 \text{ MPa}$. Let $n_b = 2.5$, then σ_a will be 130 MPa and the maximum stress arising in the winding cradle is 49 MPa which will be 2.6 times less than σ_a .

The value of the reserving strength coefficient $n_b = 320/49 = 6.5$ exceeds the necessary value $n_b = 2.5$. At a more detailed studying, the sizes of the cradle walls could be optimized.

4.1.2. INTERNAL FRAME

The frame for the first type modules is an octagonal figure (see Fig.41). Each side of this figure is a bar with radius r and length $l = 0.35 \text{ m}$. The force $P_1 = P/2 \sin \alpha$ acts on the bar, where $P = 519 \text{ kN}$ and $\alpha = 22.5^\circ$, and we have $P_1 = 683 \text{ kN}$. There is an equivalence scheme of loading in Fig.45.

In this case, the length of the bar is decreased by

$$\Delta l = P_1/EF. \quad (1)$$

Let us suppose the value of displacement to be $\Delta l = 2 \cdot 10^{-4} \text{ m}$. We get from formula (1) the cross-section of the bar: $F = 1.7 \cdot 10^{-2} \text{ m}^2$, and r will be 0.08 m .

The maximum stress is $\sigma_{max} = P_1/F$, $\sigma_{max} = 34 \text{ MPa}$.

For the second type of module the frame has the bars of length $l = 0.09 \text{ m}$. The force $P_2 = 1383 \text{ kN}$ acts on the bar. The length decrement is $\Delta l = 1 \cdot 10^{-4} \text{ m}$, and so $F = 1.82 \cdot 10^{-2} \text{ m}^2$, $r = 0.76 \text{ m}$ and the maximum value $\sigma_{max} = 79 \text{ MPa}$.

The second variant. The internal frame is a ring (Fig.46) with middle radius $R = 0.11 \text{ m}$, cross-section $b = 0.1 \text{ m}$, $h = 0.085 \text{ m}$ and $F = 0.0085 \text{ m}^2$.

The moment of the ring inertia is:

$$J = bh^3/12, J = 5.12 \cdot 10^{-6} \text{ m}^4.$$

The section modules:

$$W = bh^2/6, W = 1.2 \cdot 10^{-4} \text{ m}^3.$$

The forces of the magnet winding are transferred to the ring, each force being 1020 kN .

The bending moment is:

$$M = ql^2/8, M = 135 \text{ MN}\cdot\text{m}.$$

The maximum stress is:

$$\sigma_{max} = 112 \text{ MPa}.$$

The radial displacement of the surface points with the loaded force, is:

$$\delta = PR_{av}^2 \left[\frac{2}{\alpha} - \frac{1}{\sin \alpha} - \frac{\cos \alpha}{\sin^2 \alpha} \right] / 2EJ,$$

$\alpha = \pi/8$, [13, Table 36, p.386],

$$\delta = 0.5 \cdot 10^{-4} \text{ m}.$$

4.1.3. EXTERNAL FRAME

This frame is also an octagonal figure (see Fig.41) consisting of bars with radius r and $l = 1.9 \text{ m}$. The force P acting on bar is $P_3 = P/2 \sin \alpha$, where $\alpha = 22.5^\circ$, $P = 245 \text{ kN}$. The equivalence scheme of loading is in Fig.45.

Let us consider $\Delta l = 4 \cdot 10^{-4} \text{ m}$, then the cross-section is

$$F = P_3 l / E \Delta l, F = 1.7 \cdot 10^{-2} \text{ m}^2, r = 0.07 \text{ m}.$$

The maximum stress is: $\sigma_{max} = 14.9 \text{ MPa}$.

From the estimated calculations we can conclude that this construction will have invariable form of winding and relative position.

The common weight of the cold part of the module is

$$Q_{common} = 8Q_1 + 12Q_2 + 12Q_3 + 8Q_4, \text{ where}$$

Q_1 is weight of winding cradle 1.72 kN ,

Q_2 — weight of internal frame 1.56 kN ,

Q_3 — weight of external frame 6.7 kN ,

Q_4 — weight of winding with a cooling tube 6.8 kN .

$$Q_{common} = 32 \text{ kN}.$$

4.1.4. VACUUM ENCLOSURE OF SC MAGNET

The vacuum enclosure consists of a duct enveloping the module winding round the periphery and of connecting tubes placed where supports are attached to the cradle (Fig.47).

To get liquid helium temperature, it is necessary to create the rarefaction $1.3 \cdot 10^{-3} \text{ Pa}$. At the vacuum enclosure the loading distributed for all the surface will be $q = 0.1 \text{ MPa}$.

Here we find the thickness h of the walls.

The equivalence scheme of loading is given in Fig.48. Here we consider a plate freely supported on each of 4 sides with sizes $a = 0.5 \text{ m}$, $b = 12 \text{ m}$. The value of the flexure can be derived from $\omega = K_\omega qa^4/Eh^3$, where E is the modulus of elongation for the alloyed steel $E = 2.1 \cdot 10^5 \text{ MPa}$, K_ω is the coefficient from the table, $K = 0.1422^{[11]}$. From this formula we can find h . If we know the value of the flexure $\omega = 0.005 \text{ m}$, then $h = 0.009 \text{ m}$.

Let us take the wall thickness of vacuum enclosure equal to $h = 0.01 \text{ m}$.

The maximum stress is $\sigma_{max} = K_\sigma qa^2/h^2$, $\sigma_{max} = 190 \text{ MPa}$.

4.2. COMPUTER MODELING OF ARISING STRESSES AND DISPLACEMENTS AT STORS CONSTRUCTION

FSTORS subroutine was used for computer modeling. This program allows one to define the stress and displacement of pondermotor forces under action.

On solving the system of equations:

$$[K]\{V\} = \{f\},$$

where $[K]$ — matrix of strength of construction, $\{V\}$ — vector of node displacement, $\{f\}$ — vector of arising forces^[14], the subroutine gives $\{V\}$ both as an array of numbers and as a graphical image of construction after the corresponding forces were involved.

The both modules were calculated separately. The data for calculation were accepted from Table 1 and Fig.40.

For the first type module the following results have been obtained:

1. the maximum deflection of the internal straight-line segment of the cradle is $1.3 \cdot 10^{-4}$ m and the maximum stress is 25 MPa;
2. the maximum deflection of the external straight-line segment of the cradle is $3 \cdot 10^{-5}$ m and the maximum stress is 2 MPa;
3. the maximum deflection of the curve-line segment of the cradle is $2 \cdot 10^{-4}$ m and the maximum stress is 60 MPa.

For the second type module, other results have been obtained:

1. the maximum deflection of the internal straight-line segment of the cradle is $1 \cdot 10^{-4}$ m and the maximum stress is 36 MPa;
2. the maximum deflection of the external straight-line segment of the cradle is $3 \cdot 10^{-5}$ m and the maximum stress is 2 MPa;
3. the maximum deflection of the curve-line segment of the cradle is $3.2 \cdot 10^{-4}$ m and the maximum stress is 160 MPa.

The pictures of the cradle deformation for the first and second types of modules, accordingly, are shown in Figs.49, 50 (dotted line gives a non-deformed cradle; deflections are represented without scale).

We see that the obtained results confirm the conclusions from Part 4.1.

5. CONCLUSIONS

A sketch design of STORS machine SCMS has been carried out whereby the main parameters of windings and elements of the magnet construction were chosen. The algorithm of the program to calculate the magnetic field induction for the whole region of the spectrometer, has been created. This algorithm takes into account mutual influence of the magnet modules. Besides, variations of the field under construction deviations in the limit range of the sizes of winding, have been obtained. Control evaluations of strength and stiffness of

constructions for constructive carrying elements have been done. Critical tensions in the winding elements were found. It has been shown that these tensions are large enough to select a greater tension in the power framework.

From this work we may conclude that there is a possibility to create a superconductor toroidal magnet with selected configuration and sizes. In the process of working design it is necessary to find the final optimal parameters and sizes of the magnet.

Calculations have shown that it is necessary to measure and control the magnetic field at many points, especially near the internal winding part, where the influence of winding size errors of calculations is large.

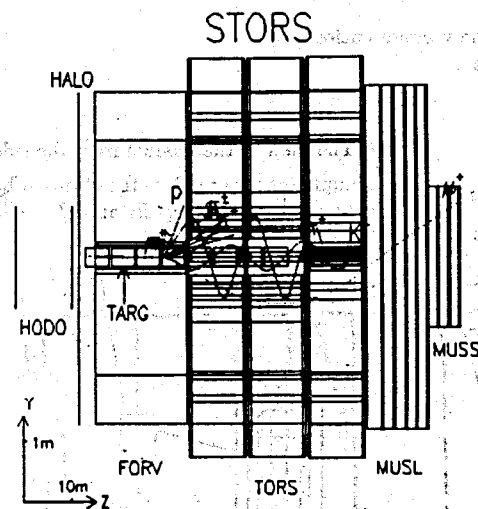


Fig.1. The scheme of superconducting toroidal spectrometer STORS (in profile):

- HODO — hodoscope scintillation planes;
- HALO — hodoscope scintillation plane to protect from beam halo;
- TARG — targets (solid and liquid);
- FORV — forward spectrometer;
- TORS — toroidal magnet spectrometer;
- MUSL, MUSS — muon identifiers

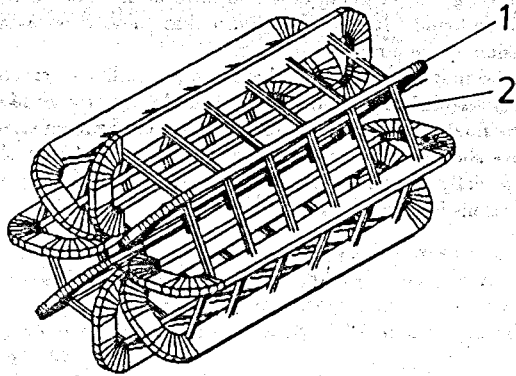


Fig. 2. The start module of the superconducting magnet in the STORS construction.

- 1 — the winding in the vacuum enclosures,
- 2 — the strength bars

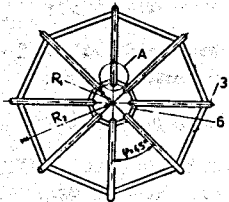


Fig. 3A. The view of the module from the side.
3 — vacuum enclosure, 6 — the strength bars in the vacuum enclosures, R_1 and R_2 — internal and external winding radii

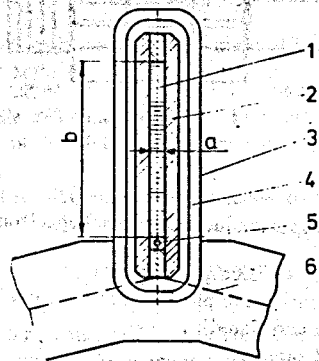


Fig. 3B. The cross-section of the magnet (place A, Fig. 3A).

- 1 — winding, 2 — box, 3 — vacuum enclosure, 4 — vacuum isolation, 5 — liquid helium pipe, 6 — the strength bars in the vacuum enclosures,
- a — width, b — height of the winding

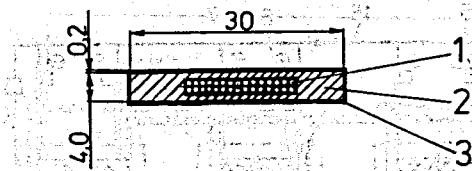


Fig. 4. The tire cross-section.

- 1 — the superconducting wire with diameter $8,5 \cdot 10^{-4} m$, 2 — stabilizing aluminium tire,
- 3 — electric insulator

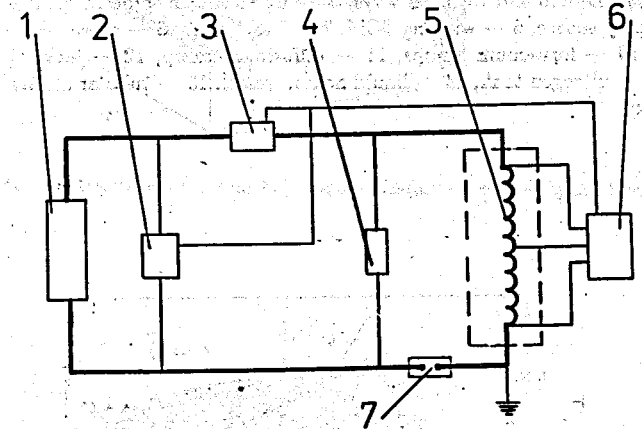


Fig. 5. The principal electricity and protection source scheme of the superconducting magnet module.

- 1 — supply source, 2 — force commutator (closed normally), 3 — danger commutator (open normally), 4 — resistivity absorber, 5 — superconducting winding, 6 — normal zone appearance detector, 7 — measurement resistor

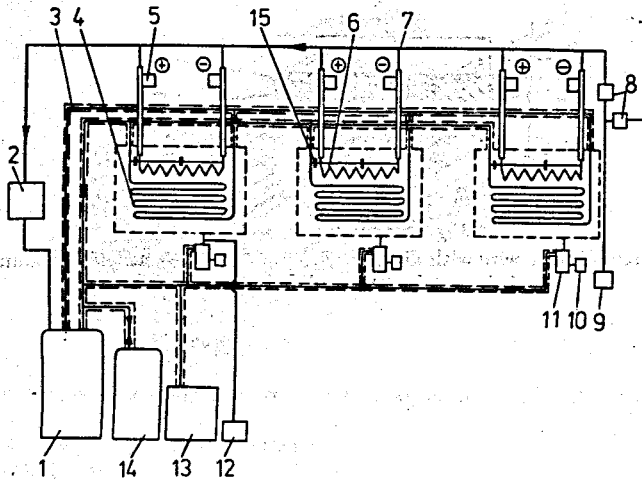


Fig.6. The principal technological scheme of the cryogenic and vacuum systems SCMS:
 1 — cryogenic helium construction CHS-1600/4.5, 2 — compressor, 3 — liquid helium and nitrogen ways, 4 — liquid helium pipe in module, 5 — supply source, 6 — winding SCM, 7 — "hot" ways, 8 — preserve switches, 9, 10 — forvacuum pumps, 11 — diffusional pump, 12 — leak detector, 13 — nitrogen tank, 14 — liquid helium vessel, 15 — tubular electric insulator

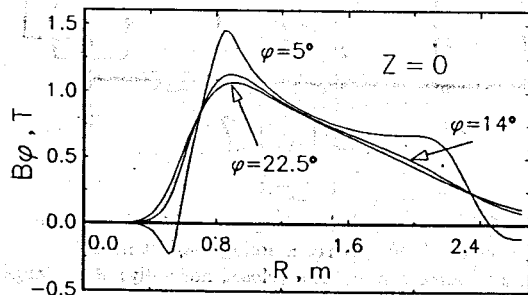


Fig.7. The radial distribution of azimuthal magnetic field component for 1 type module

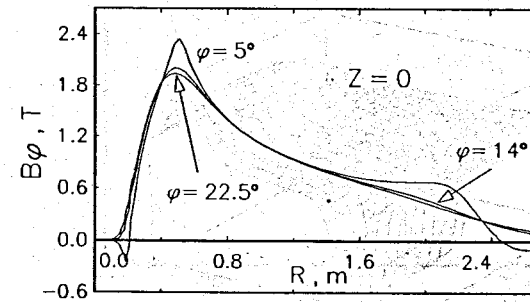


Fig.8. The radial distribution of azimuthal magnetic field component for 2 type module

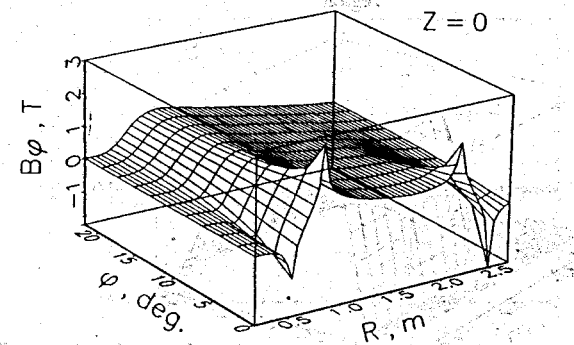


Fig.9. The space distribution of azimuthal magnetic field component in midplane

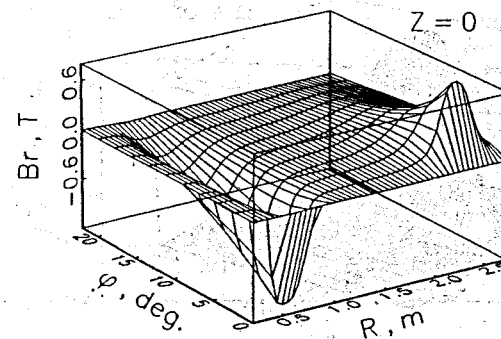


Fig.10. The space distribution of radial magnetic field component in midplane

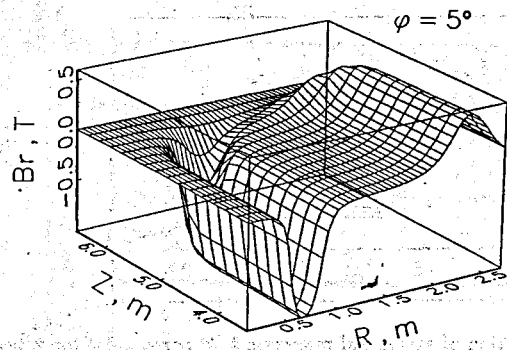


Fig.11. The space distribution of radial magnetic field component in the border module region

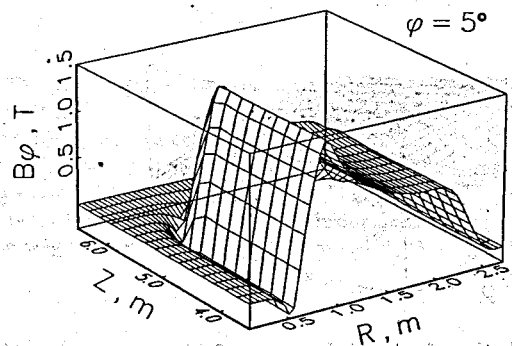


Fig.12. The space distribution of azimuthal magnetic field component in the border module region

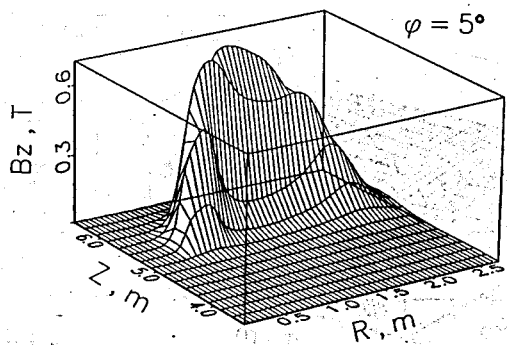


Fig.13. The space distribution of axial magnetic field component in the border module region

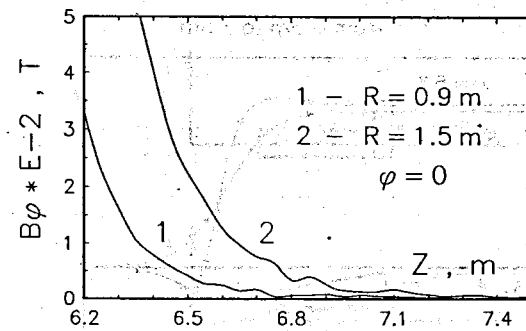


Fig.14. The axial distribution of azimuthal magnetic field component near module

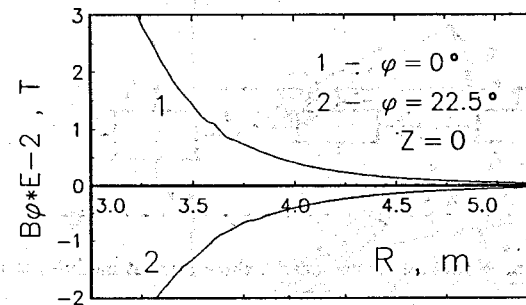


Fig.15. The radial distribution of azimuthal magnetic field component near module

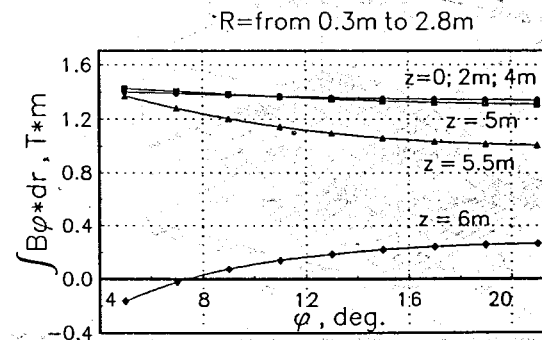


Fig.16. The integral of the azimuthal magnetic field component along radius for $z = const.$

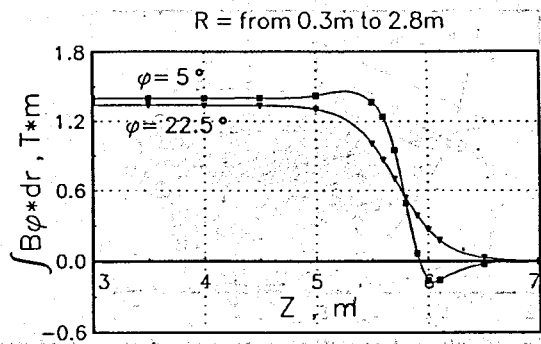


Fig.17. The integral of the azimuthal magnetic field component along radius for $\varphi = const$

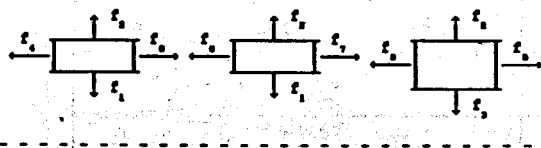


Fig.18. The force scheme of mutual disposition for three magnet modules of the STORS

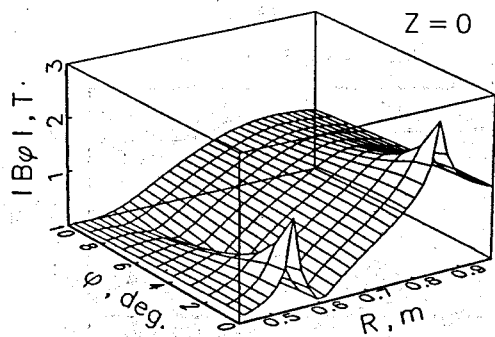


Fig.19. The space distribution of azimuthal magnetic field component in the current region of winding

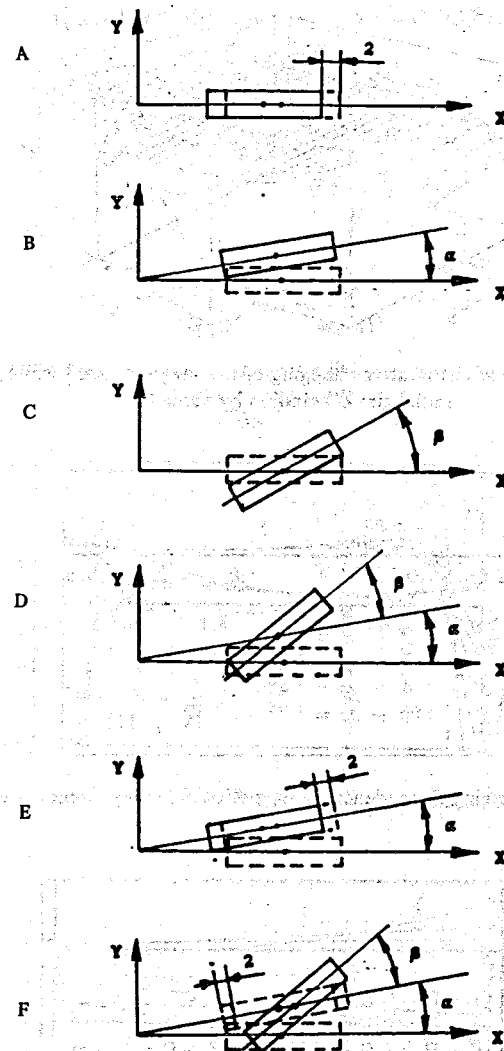


Fig.20. The reliable deviation variants in module construction

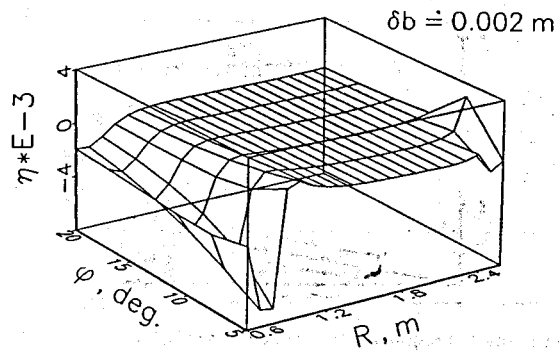


Fig.21. The character of the relative changing of the magnetic field while changing the radial size of winding by value δb

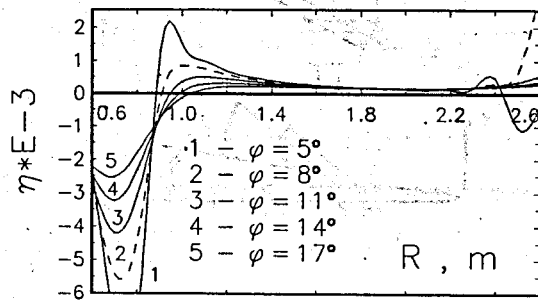


Fig.22. The relative changing dependence of magnetic field on radius for the case shown in Fig.21

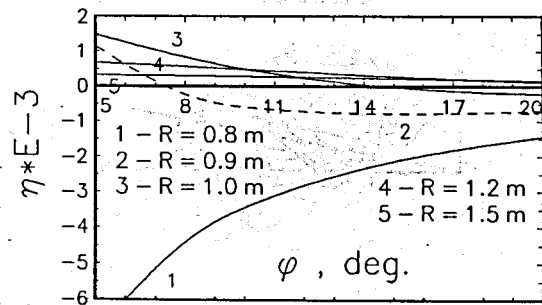


Fig.23. The relative changing dependence of magnetic field on azimuth for the case shown in Fig.21

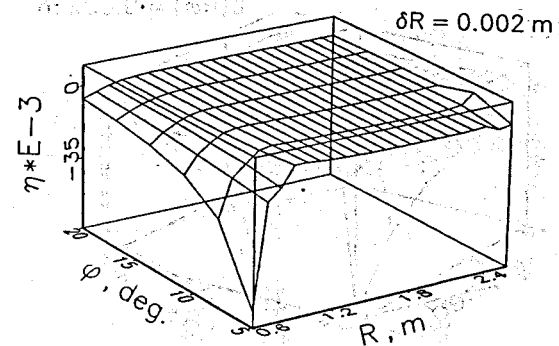


Fig.24. The relative changing character of magnetic field while winding displacement along radius by value δR

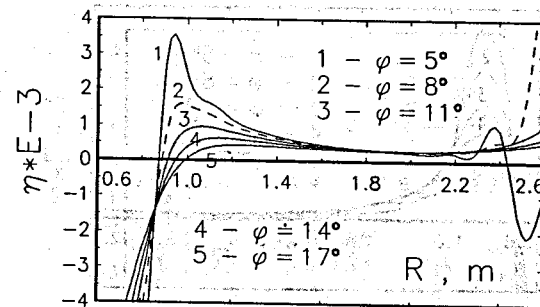


Fig.25. The relative changing dependence of magnetic field on radius for the case shown in Fig.24

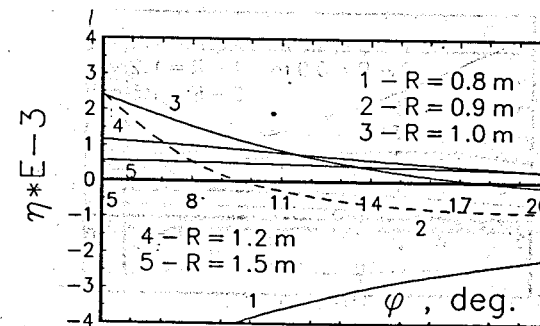


Fig.26. The relative changing dependence of magnetic field on azimuth for the case shown in Fig.24

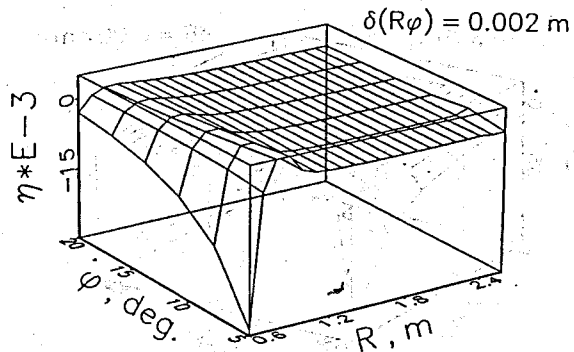


Fig.27. The relative changing character of the magnetic field in case of the angle displacement of winding plane by value $\alpha = 0.135^\circ$

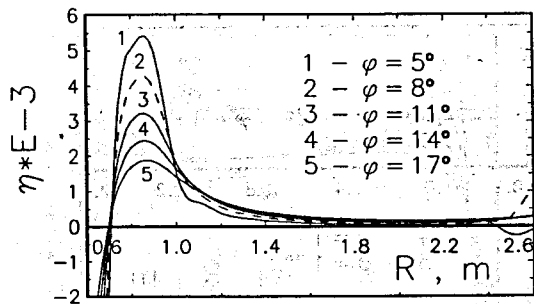


Fig.28. The relative changing dependence of magnetic field on radius for the case shown in Fig.27

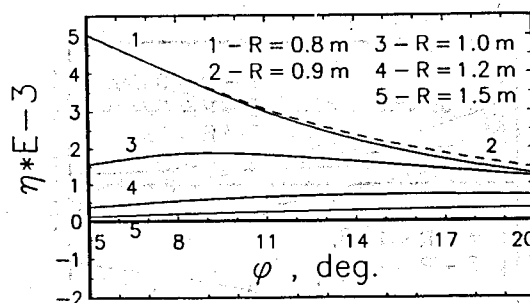


Fig.29. The relative changing dependence of magnetic field on azimuth for the case shown in Fig.27

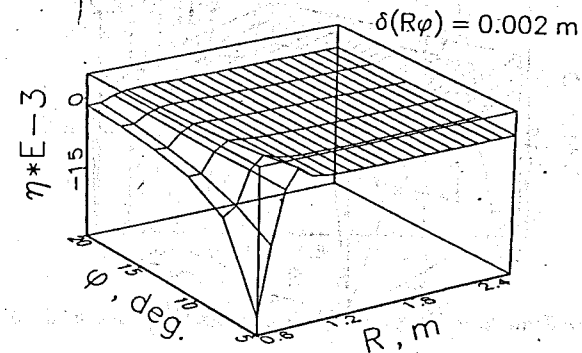


Fig.30. The relative changing character of magnetic field in case of the winding bend near its own axis by value $\beta = 0.744^\circ$

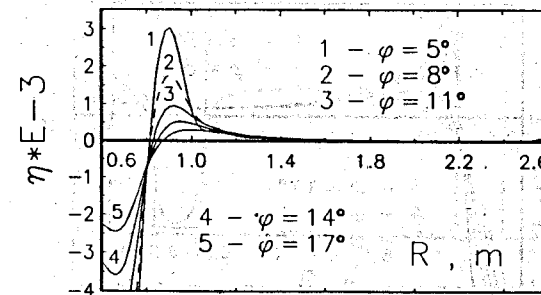


Fig.31. The relative changing dependence of magnetic field on radius for the case shown in Fig.30

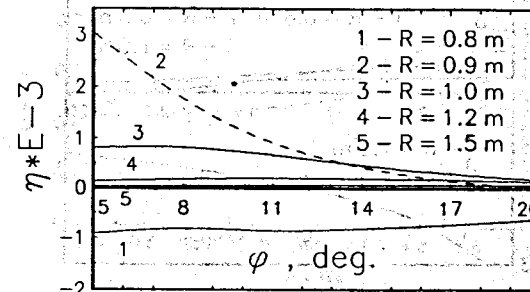


Fig.32. The relative changing dependence of magnetic field on azimuth for the case shown in Fig.30

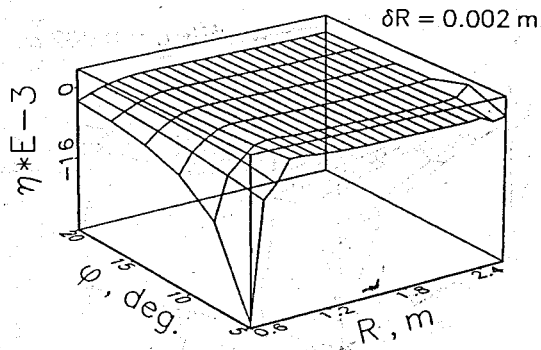


Fig.33. The relative changing character of magnetic field in case of non-parallelism of winding axial segments by value δR

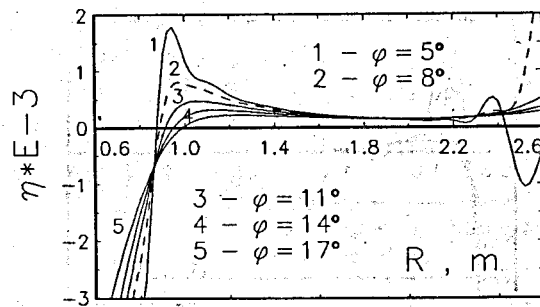


Fig.34. The relative changing dependence of magnetic field on radius for the case shown in Fig.33

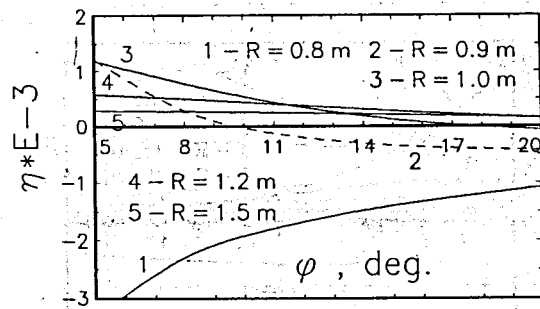


Fig.35. The relative changing dependence of magnetic field on azimuth for the case shown in Fig.33.

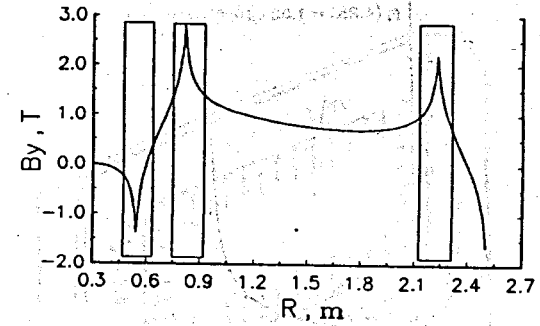


Fig.36. The usual B_y magnetic field type along radius at small angles

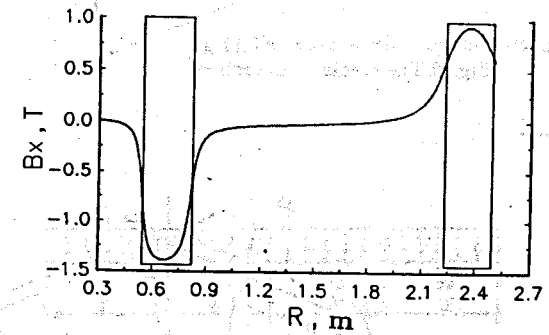


Fig.37. The usual B_x magnetic field type along radius at small angles

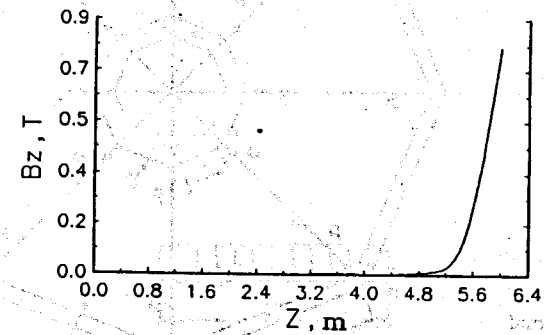


Fig.38. The usual B_z magnetic field type along z

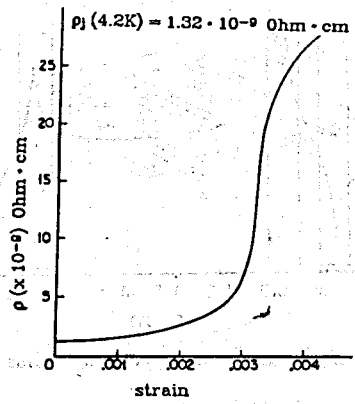


Fig.39. The electric resistance after 1000 cycles of loading depending on value of high pure aluminium relative strain. Initial RRR of aluminium is equal to 2000^[9]

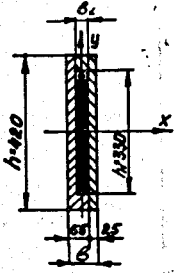


Fig.40. The cradle cross-section

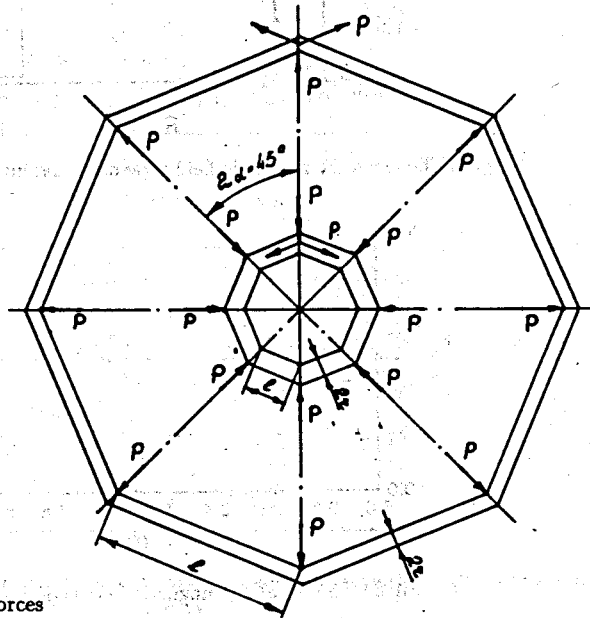


Fig.41. The external and internal frames of module and arising forces

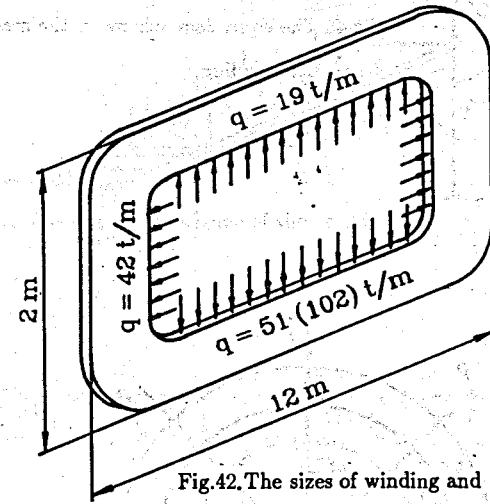


Fig.42. The sizes of winding and arising forces

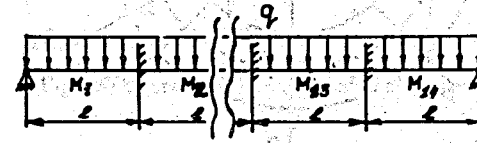


Fig.43. The loading of the internal and external straight-line segments of winding

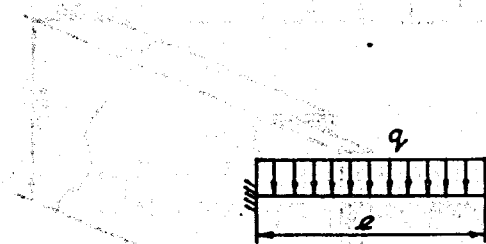


Fig.44. The loading of the vertical straight-line segments of winding

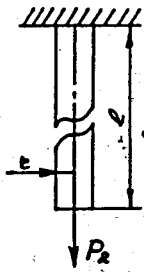


Fig.45. The equivalent scheme of the magnet frame bars loading

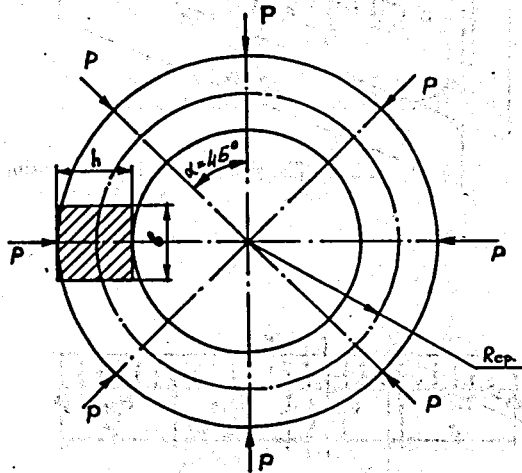


Fig.46. The internal frame of the second type (ring) and its scheme of loading

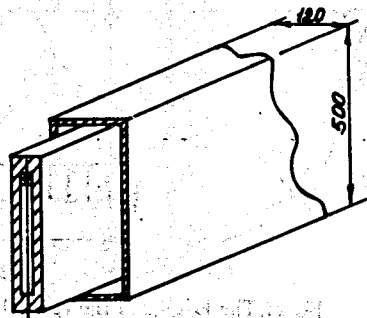


Fig.47. The vacuum enclosure of winding

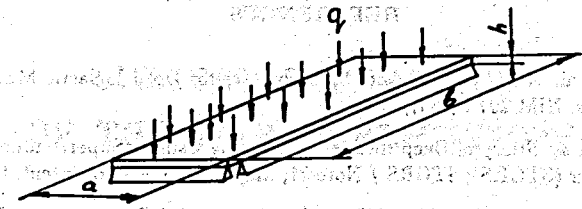


Fig.48. The equivalent scheme of the vacuum enclosure segment loading

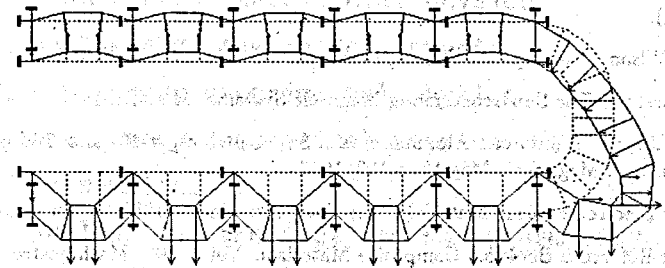


Fig.49. The cradle deformation of the 1 type module

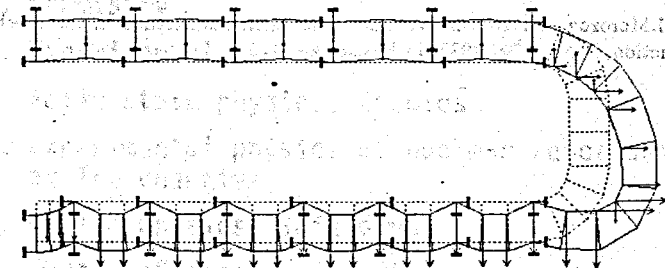


Fig.50. The cradle deformation of the 2 type module

REFERENCES

1. D.Bollini et al. A High Luminosity Spectrometer for Deep Inelastic Muon Scattering Experiments, NIM 204 (1983), 333.
2. G.Guoyot et al. Study of Deep Inelastic Scattering Using a Superconducting Toroidal Spectrometer (STORS); STORS / Note 91, May 1991; Letter of Intent, Geneva, 1991.
3. Z.V.Borisovskaya et al. MAGSYS — the Complex of Programs for Calculating of Three-Dimensional Magnetostatic Fields for the Cyclotron and Synchrotron Magnetic System. JINR, B1-9-85-232, Dubna, 1985 (in Russian).
4. P.F.Koshelev. The Mechanical Property of Alloys for Cryogenic Technique. M.: Mashinostroenie, 1971 (in Russian).
5. P.I.Orlov. The Construction Beginning. Vol.1. M.: Mashinostroenie, 1988 (in Russian).
6. M.Wilson. The Superconducting Magnets. M.: Mir, 1985 (in Russian).
7. G.Brehna. The Superconducting Magnetic Systems. M.: Mir, 1976 (in Russian).
8. H.R.Segal. Reinforced Aluminum as a Superconducting Magnet Stabilizer. IEEE Trans. on Mag., Vol. Mag-13, p.109, 1977.
9. The Electrotechnique Materials. M.: Energoatomizdat, 1983 (in Russian).
10. The Reference Book for Composite Materials. Vol.1. M.: Mashinostroenie, 1988 (in Russian).
11. I.A.Birger, B.F.Shorr, G.B.Iosilevitch. The Strength Calculating of the Components of Machines, M.: Mashinostroenie, 1979 (in Russian).
12. A.P.Yakovlev, V.V.Matveev, G.S.Piskalenko. The Reference Book for the Material Resistance, Kiev: Naukova Dumka, 1988 (in Russian).
13. V.L.Agairov, A.A.Amel, L.E.Andreeva. The Reference Book of Machine-Builder, M.: Mashgiz, 1962 (in Russian).
14. E.M.Morozov, G.P.Nikishkov. The Final Elements Method in the Mechanics of Destruction, M.: Nauka, 1980 (in Russian).

Received by Publishing Department
on December 7, 1993.